THE ASTROPHYSICAL JOURNAL, 469:L33–L36, 1996 September 20

FIRST RESULTS FROM THE ALL-SKY MONITOR ON THE *ROSSI X-RAY TIMING EXPLORER*

ALAN M. LEVINE,[1] HALE BRADT,[1,2] WEI CUI,[1] J. G. JERNIGAN,[3] EDWARD H. MORGAN,[1]
RONALD REMILLARD,[1] ROBERT E. SHIREY,[1,2] AND DONALD A. SMITH[1,2]
Received 1996 May 29; accepted 1996 July 9

ABSTRACT

The all-sky monitor on the *Rossi X-Ray Timing Explorer* has been monitoring the sky in the 1.5–12 keV band since late February. The instrument consists of three coded-aperture cameras that can be rotated to view different regions by a motorized drive assembly. Intensities of ~100 known sources are obtained via least-squares fits of shadow patterns to the data and compiled to form X-ray light curves. Six orbital periodicities and four long-term periodicities, all previously known, have been detected in these light curves. Searches for additional sources have also been conducted. X-ray light curves for the Crab Nebula, Cyg X-1, 4U 1705−44, GRO J1655−40, and SMC X-1 are reported. They illustrate the quality of the results and the range of observed phenomena.

Subject headings: instrumentation: detectors — X-rays: general — X-rays: stars

1. INTRODUCTION

The all-sky monitor (ASM) on the *Rossi X-Ray Timing Explorer* (*RXTE*) is now monitoring the highly variable and often unpredictable X-ray sky. In the tradition established by the all-sky monitors on the *Vela 5B*, *Ariel V*, and *Ginga* satellites (Holt & Priedhorsky 1987; Priedhorsky & Holt 1987; Tsunemi et al. 1989) and more recently by the BATSE instrument on the *Compton Gamma Ray Observatory* (Fishman et al. 1989), our results are being used to alert observers to the appearance of transients and to other time-variable phenomena and to record long-term intensity histories of bright X-ray sources. Herein we briefly describe the instrument and data analysis and illustrate the results with selected light curves.

2. INSTRUMENTATION

The ASM consists of three Scanning Shadow Cameras (SSCs) mounted on a motorized rotation drive. Each SSC contains a position-sensitive proportional counter (PSPC) that views the sky through a slit mask (Fig. 1). The PSPC is used to measure the displacements and strengths of the shadow patterns cast by X-ray sources within the field of view (FOV) and thereby to infer the directions and intensities of the sources.

The mask is a thin aluminum sheet that is subdivided into 6×2 subsections. Each of the 12 subsections contains ~15 open and ~16 closed slit elements of size 1 by 110 mm arranged in one of six carefully chosen pseudorandom patterns. The 1 mm width of an element near the center of the mask subtends 12′ at the PSPC.

The volume between the slit mask and the PSPC is divided into two halves by a partition so that each half of the PSPC views the sky only through half (6×1 subsections) of the mask. This yields a FOV of 6° by 90° FWHM (12° × 110° FWZI).

Each PSPC contains eight resistive carbon-coated quartz fiber anodes, each end of which is connected to a dedicated electronic measurement chain. An X-ray event detected in the volume surrounding one of these anodes yields a pair of pulse heights, which are used to compute the event energy and position (i.e., the coordinate perpendicular to the slits in the mask) via the charge-division technique. The achieved position resolution is 0.2–0.5 mm, depending on photon energy. Each PSPC also contains 12 metal anodes that are used to veto events caused by charged particles.

X-rays must penetrate through an 8 μm thick aluminized plastic thermal shield and a 50 μm thick beryllium window to enter the PSPC. The PSPCs in SSCs 2 and 3 also have a thin (~2 μm) coating of polyimide on the interior of the beryllium foil for protection against possible leaks. The X-rays are absorbed in a 95% xenon–5% CO_2 gas mixture (total pressure 1.2 atm). Each SSC is sensitive in the energy range of approximately 1.5–12 keV, with on-axis effective areas of ~10 cm^2, ~30 cm^2, and ~23 cm^2 at 2, 5, and 10 keV, respectively.

Event data are normally compressed within the two ASM Event Analyzers (EAs) in the Experiment Data System and relayed to the spacecraft for insertion in the telemetry stream. One ASM EA accumulates histograms of counts binned as a function of position for each of the resistive anodes and for each of three energy bands roughly corresponding to 1.5–3, 3–5, and 5–12 keV. These position histograms are accumulated in series of ~90 s "dwells." During each dwell, the spacecraft maintains a fixed attitude and the ASM rotation drive, which is also controlled by this EA, is not active, so that the orientation of each SSC is fixed in relation to the sky. A position histogram thus contains the superposition of the mask shadows from each X-ray source in the FOV during a single dwell (Fig. 2). The start times and rotation drive angles for each dwell and high-voltage on/off commands are planned in advance on the ground to minimize Earth occultations and to avoid operation under conditions which may present extra risk to the PSPCs (see below).

The other ASM EA produces count rates for both X-ray ($\frac{1}{8}$ s time bins) and background (1 s time bins) events and pulse-height spectra (64 s time resolution, 64 channels for 0–20 keV).

When the high-voltage supplies of the SSCs were first activated on 1996 January 5, the entire ASM operated normally. However, on the next day, SSC 3 developed high-voltage breakdown to two adjacent carbon-coated quartz

[1] Center for Space Research, Massachusetts Institute of Technology, Cambridge, MA 02139.
[2] Department of Physics, Massachusetts Institute of Technology, Cambridge, MA 02139.
[3] Space Sciences Laboratory, University of California, Berkeley, CA 94720.

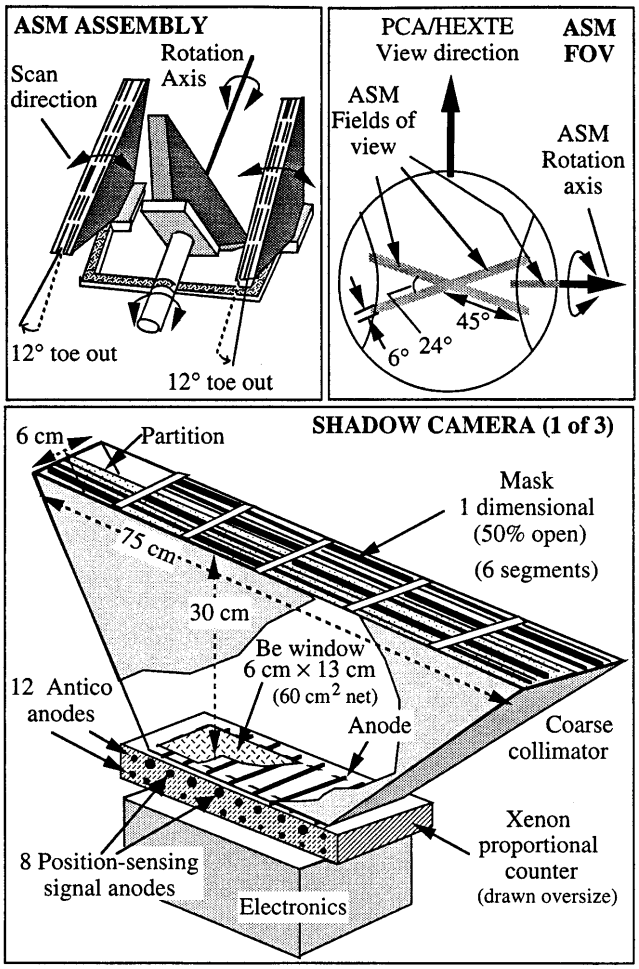

FIG. 1.—*Top left*: Schematic diagram showing the relative orientations of the SSCs as configured on the ASM. *Top right*: The centers of the fields of view (FOVs) of SSC 1 and SSC 2 are approximately co-aligned perpendicular to the ASM rotation axis. The long axes of their FOVs are tilted by +12° and −12° relative to the rotation axis. The center of the FOV of SSC 3 is pointed parallel to the rotation axis. The view direction of the other two *RXTE* instruments is indicated. *Bottom*: Schematic diagram of an SSC illustrating the major components. One subsection of the mask is actually nearly as long as the Be window.

anodes, and on January 12, SSC 2 developed similar breakdown on one anode. All three PSPCs were then turned off so the problems could be investigated. No cause for the breakdown events was identified. However, procedures were adopted to avoid operations in additional high-background regions and whenever the Sun with its high X-ray flux could be in the FOV. Both malfunctioning PSPCs were recovered by letting the breakdown proceed until it largely ceased, probably because of the discharge eroding the carbon from the entire lengths of the affected anodes. "Normal" operation commenced for SSC 1 with all eight anodes on February 22, for SSC 2 with seven anodes on March 12, and for SSC 3 with six anodes on March 19. Since these dates, the operation has been essentially continuous except for a few days when operational difficulties intervened. Currently, the ASM collects useful data with a duty cycle of ~40%. This duty cycle, together with spacecraft maneuvers that are planned to carry out the observing program of the other *RXTE* instruments, produces a highly stochastic pattern of sky coverage with a randomly chosen source being scanned typically five to 10 times per day.

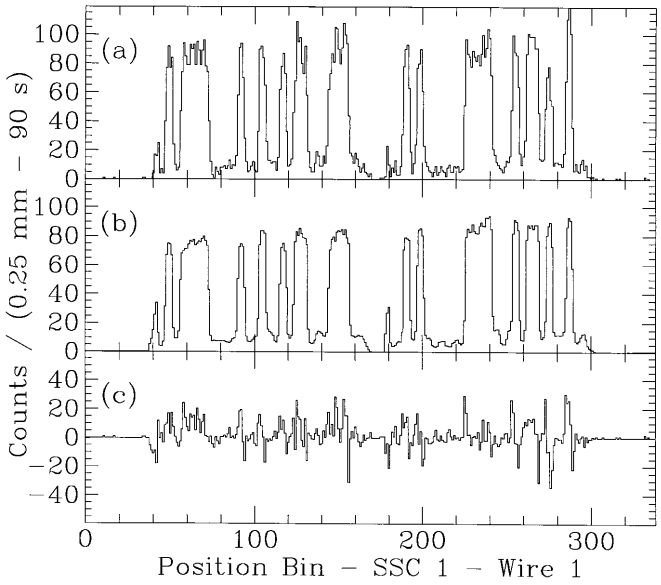

FIG. 2.—(*a*) Position histogram obtained 1996 April 19 with Sco X-1 at −0°.67, 23°.0 from the center of the FOV in the narrow and long directions, respectively. There were also 10 other sources from the active catalog in the field, but the brightest of these was ~7% as bright as Sco X-1. One position bin corresponds to a region of width ~0.25 mm. (*b*) Model histogram and (*c*) residuals, i.e., the difference between the observed data and the model. The magnitude of the residuals illustrates a need to improve the histogram model by refining calibration parameters. The reduced χ^2 statistic for the fit of the data from all eight anodes is 1.87.

The gain of the three PSPCs has remained stable to ~1% since launch, as determined by measurement of 6 keV X-rays from weak ^{55}Fe calibration sources.

3. DATA ANALYSIS

The analysis proceeds by computing intensities for sources listed as active in a master catalog and then by searching for and locating additional sources. The master catalog includes all X-ray sources with accurate positions (uncertainty <3′) and recorded instances of X-ray flux >3 mCrab at 2–10 keV. Many of these sources are transient in nature and may be below the ASM detection threshold for years at a time. Therefore, the catalog flags as active only the sources we may expect to detect with the ASM. This helps avoid needless problems with source confusion and computation time.

Source intensities are obtained from the solution of a linear least-squares fit of position histograms with model shadow patterns for each active source within the field of view and with patterns representing non–X-ray and diffuse X-ray backgrounds (cf. Doty 1988). The amplitudes of the patterns are taken as free parameters. First, an unweighted fit is computed. The fit is then iterated twice using as weights the reciprocals of the variances of the counts per bin expected from the solution computed in the previous iteration. The fit solution also yields estimates of the uncertainties of the derived intensities; these uncertainties are based purely on the photon counting statistics predicted by the best-fit model.

Two types of problems with the analysis are currently addressed as follows. First, the fit is repeated with sources whose fitted intensities are below two standard deviations being removed one at a time until no more such intensities are obtained from the fit. This is done to eliminate negative fitted source intensities from the model and also to help reduce

problems of confusion in crowded fields. The fitted intensity and the associated statistical uncertainty for each source is saved from the last solution in which it is listed. Second, the fitting process is repeated with small adjustments being made to the pointing direction of the SSC, since calibration of the SSC pointing directions and rotation drive angle sensors is not yet sufficiently accurate for the most demanding cases (e.g., with Sco X-1 in the field). Source intensities and errors (and estimated adjustments to the pointing direction) are reported from the fit with the minimum value of the reduced χ^2 statistic.

The fit residuals (see Fig. 2) are examined via a cross-correlation technique for evidence of sources beyond those from the active list. When such a source is detected, the cross-correlation function is used to estimate its celestial location. Since the location derived from a single dwell of one SSC is long and narrow ($\sim 5' \times 5°$ for a $\sim$100 mCrab source), this is best done using the intersections of error boxes from multiple dwells and SSCs. The derived location is used to attempt to identify the source with objects flagged as inactive in the master catalog. The coordinates from the analysis or from the catalog listing (if the source was successfully identified) are entered into the active catalog, and the fit procedure is repeated.

To date, this analysis has been performed on a dwell-by-dwell and SSC-by-SSC basis but may be extended to data from multiple dwells and SSCs.

Fitted intensities are normalized to on-axis count rates in SSC 1. This requires two corrections, the first of which must be applied because the position histogram models computed for unit count rate sources do not yet fully take into account the loss of effective area for sources at large elevations in the FOV. At present, this correction factor has been empirically determined from observations of the Crab Nebula. The second correction accounts for absorption in the polyimide coating on the windows of SSC 2 and SSC 3, so that the results from all three SSCs are consistent.

4. RESULTS

The fitted intensities depend upon the accuracy of the model of the shadow patterns and upon spectrum-dependent differences among the SSCs and individual anodes. The model patterns are based upon both laboratory and in-orbit calibrations. There are still small systematic differences between the measured position histograms and the models (Fig. 2). We will continue to refine the models.

The corrected intensities in the 1.5–12 keV band from individual dwells are selected so as to reject results from fits with high values of reduced χ^2, short exposures due to entry into high-background regions, sources close to or behind Earth's limb, sources close to the edge of the FOV, or fields that are exceptionally crowded. The remaining intensities are plotted in light curves of each of $\sim$100 sources. One-day averages have also been plotted. Selected light curves are shown in Figure 3.

The intensities for the Crab Nebula have an apparent scatter about the mean of $\sim$5% (Fig. 3), of which $\sim$4% can be attributed to count statistics. This indicates that intensities of bright sources in uncrowded fields are typically affected by systematic errors of $\sim$3%. Such systematic effects are represented in all sources (>10 σ) by adding an uncertainty corresponding to 3% of the intensity in quadrature with the counting statistical uncertainty.

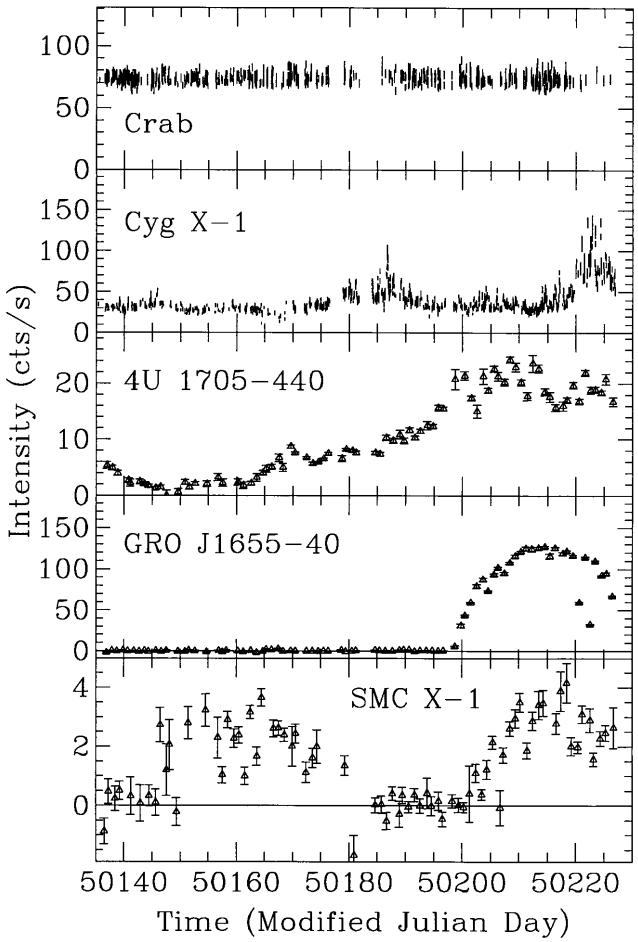

FIG. 3.—X-ray light curves (1.5–12 keV) for the Crab Nebula, Cyg X-1, 4U 1705−44, GRO J1655−40, and SMC X-1. The light curves for the Crab Nebula and Cyg X-1 comprise measurements from individual dwells. The bottom three light curves comprise intensities from individual dwells averaged in 1 day time bins. The error bars represent ± 1 σ statistical uncertainty added in quadrature with a simple estimate of systematic errors (see text). MJD 50082.0 is equivalent to 1996 January 0.0 UT.

Other sources may be affected by systematic errors beyond the level apparent in the Crab Nebula light curve. First, there are likely to be additional systematic effects upon the intensity of a source when other sources, particularly bright ones, are also in the FOV. Our results for Sco X-1 indicate that other sources in the field may be affected at the level of a few percent (of Sco X-1). Second, incompleteness of the active catalog can lead to errors. Third, low energy absorption by the window and thermal shield increases with elevation of a source in the FOV. Currently, the elevation corrections are based on the integrated 1.5–12 keV Crab flux only. Sources with markedly different spectra could have additional scatter in the light curves. We caution the reader to remain aware of the above qualifications when using either the results from selected sources, which we now present, or the comprehensive set of results available elsewhere.

The light curve of Cygnus X-1 (Fig. 3) shows variability that is more evident with the time resolution of the measurements from individual dwells (as shown) than in 1 day averages (not shown). In particular, the increase to $\sim$1.3 Crab for a brief time ($<$1 day) around MJD 50187 is not nearly as apparent in the 1 day averages, where the peak intensity is $\sim$0.75 Crab.

The strengthening to ~2 Crab around MJD 50220 is apparently a transition to the high state (van der Klis 1995); the spectrum appears to soften as the intensity increases. A light curve of much longer duration and a time resolution of days has been presented by Priedhorsky, Terrell, & Holt (1983). We note that occasions with the intensity as bright as 1.3 Crab are unusual, at least in time averages of 1 day or longer.

The low-mass X-ray binary 4U 1705−44 is seen to vary from <25 mCrab to ~300 mCrab (Fig. 3). Previous observers have noted variability over a similar intensity range (Langmeier et al. 1987; van Paradijs 1995). This source exhibits X-ray bursts and other aperiodic variability that appear to be correlated with the intensity state (Langmeier et al. 1987; Langmeier, Hasinger, & Trümper 1989).

No emission from the X-ray transient GRO J1655−40 above ~12 mCrab was detected with the ASM prior to MJD 50198, at which time the count rate rose to ~2 Crab over the course of ~10 days (Fig. 3). Outbursts of this source have been previously detected in 1994 and 1995 (Harmon et al. 1995; Wilson et al. 1995; Sazonov & Sunyaev 1995; Zhang et al. 1995 and references therein). This source is a dynamical black hole candidate (Bailyn et al. 1995) that manifests relativistic radio jets (Tingay et al. 1995; Hjellming & Rupen 1995). Optical and radio activity that are correlated with X-ray activity have been previously seen (Bailyn et al. 1995; Tingay et al. 1995).

The SMC X-1 light curve (Fig. 3) indicates that the source was detected in 1 day averages from MJD 50146 to about MJD 50180 and again starting at about MJD 50202. This on-off behavior is very similar to that reported previously by Gruber & Rothschild (1984), who suggested that it may be a $\sim 60^{d}$ quasi periodicity and, if so, would likely be analogous to the 35^{d} cycle of Her X-1 and the 30^{d} cycle of LMC X-4.

The larger collection of light curves includes many interesting results that cannot be presented here. For example, one can see the gradual decay in the flux of GRO J1744−28, large fluctuations in the intensities of GRS 1739−278 and GRS 1915+105, the end of an outburst of 4U 1608−52, and a flux increase in LMC X-3. The long-term periodicities of Her X-1, LMC X-4, and GX 301–2 (see references in van Paradijs 1995) are also evident.

We have searched each of the ~100 light curves for periodicities. For this purpose, the measurements from individual dwells were averaged in 0.05 day bins, and the mean count rate was subtracted from each bin that contained at least one measurement. The resulting binned light curves were transformed using a fast Fourier transform to obtain power density spectra. The power spectra have been examined for obviously significant peaks in the period range 0.1 to ~15 days. The orbital periods for six binary systems are clearly apparent in the results. These include the orbital periods of Cen X-3 ($2\overset{d}{.}1$), Cir X-1 ($16\overset{d}{.}6$), Cyg X-3 (4.8 hr), Her X-1 ($1\overset{d}{.}7$), Vela X-1 ($9\overset{d}{.}0$), and X1700−377 ($3\overset{d}{.}4$; see van Paradijs 1995). We will continue to search for periodicities as measurements are added to the light curves.

Finally, we have estimated typical sensitivities to sources in uncrowded fields from the scatter in the measurements of five sources whose light curves (not shown) indicate that they have not been detected. The result is ~35 mCrab (2 σ) for those individual dwells in which the source appears in the central half of the field of view and ~10 mCrab for the 1 day averages.

5. CONCLUSION

The ASM is producing interesting and timely results on many X-ray sources. We encourage the scientific community and all interested persons to explore and make use of the ASM results via a public archive maintained by the *RXTE* Guest Observer Facility (see the World Wide Web URL http://heasarc.gsfc.nasa.gov/docs/xte/xte_1st.html for information).

We gratefully acknowledge the essential contributions of William Mayer and Robert Goeke at MIT and also those of every member of the *RXTE* teams at MIT and GSFC to the success of the ASM and *RXTE*. The *RXTE* team at MIT was supported by NASA contract NAS5-30612.

REFERENCES

Bailyn, C. D., Orosz, J. A., McClintock, J. E., & Remillard, R. A. 1995, Nature, 378, 157
Doty, J. P. 1988, Proc. SPIE, 982, 164
Fishman, G. J., et al. 1989, in Gamma Ray Observatory Science Workshop, ed. C. R. Shrader, N. Gehrels, & B. Dennis (CP-3137) (Greenbelt, MD: NASA), 2–39
Gruber, D. E., & Rothschild, R. E. 1984, ApJ, 283, 546
Harmon, B. A., et al. 1995, Nature, 374, 703
Hjellming, R. M., & Rupen, M. P. 1995, Nature, 375, 464
Holt, S. S., & Priedhorsky, W. 1987, Space Sci. Rev., 45, 269
Langmeier, A., Hasinger, G., & Trümper, J. 1989, ApJ, 340, L21
Langmeier, A., Sztajno, M., Hasinger, G., Trümper, J., & Gottwald, M. 1987, ApJ, 323, 288
Priedhorsky, W. C., & Holt, S. S. 1987, Space Sci. Rev., 45, 291
Priedhorsky, W. C., Terrell, J., & Holt, S. S. 1983, ApJ, 270, 233
Sazonov, S., & Sunyaev, R. 1995, IAU Circ., 6209
Tingay, S. J., et al. 1995, Nature, 374, 141
Tsunemi, H., Kitamoto, S., Manabe, M., Miyamoto, S., Yamashita, K., & Nakagawa, M. 1989, PASJ, 41, 391
van der Klis, M. 1995, in X-Ray Binaries, ed. W. H. G. Lewin, J. van Paradijs, & E. P. J. van den Heuvel (Cambridge: Cambridge Univ. Press), 252
van Paradijs, J. 1995, in X-Ray Binaries, ed. W. H. G. Lewin, J. van Paradijs, & E. P. J. van den Heuvel (Cambridge: Cambridge Univ. Press), 536
Wilson, C. A., Harmon, B. A., Zhang, S. N., Paciesas, W. S., & Fishman, G. J. 1995, IAU Circ., 6152
Zhang, S. N., Harmon, B. A., Paciesas, W. S., & Fishman, G. J. 1995, IAU Circ., 6209